JMEPEG (2021) 30:9094–9107
https://doi.org/10.1007/s11665-021-06098-0

©ASM International
1059-9495/$19.00

Comparative Study between Small Punch Tests and Finite Element Analysis of Miniature Steel Specimens

Zhaoyi Cheng, Jianrong Sun, Pengfei Tai, Linqi Zhang, Yuting Wei, Hailong Chang, Rebecca Thuku, and Kelvin M. Gichuhi

Submitted: 15 September 2020 / Revised: 15 April 2021 / Accepted: 5 July 2021 / Published online: 12 August 2021

The experimental method of small punch tests (SPT) using miniature specimens has great advantages and broad application prospects for material research in space, nuclear plants and other extreme environments. However, at present, the application of this method lacks unified standards and norms, which affects its application effect. Based on these, the mechanical properties of φ3 mm disks miniature specimens of SIMP steel with different thicknesses are investigated through SPT experiments, finite element modeling (FEM) analyses and scanning electron microscopy observations. All the results demonstrate that the relationship of the mechanical properties of standard tensile test samples derived from the data of small punch test is established, and the method of establishing this mechanical relationship is also provided. Most importantly, based on the shear stress analyses of FEM calculations, most mechanical properties, such as yield strength, ultimate strength, fracture toughness and elastic modulus, can be obtained directly through SPT experiments. These findings may improve the possibility of establishing a widely accepted program for obtaining basic materials properties from SPT experimental data by using FEM simulations and provide a new comparison scheme (or norm) for obtaining accurate data from miniature specimens.

Keywords finite element modeling (FEM), mechanical testing, miniature specimens, SIMP steel, small punch tests (SPT)

1. Introduction

The service behavior of materials in extreme environments is one of the main bottlenecks restricting the use and development of nuclear energy, and the material problems determine the feasibility, safety and economy of nuclear energy systems (Ref 1). The operating environment of the nuclear energy systems is extremely harsh, in which structural materials are confronted with multi-field coupling effects such as the high temperature of the reactor core, strong radiation field, high pressure, coolant corrosion and abrasion, which will lead to embrittlement, fatigue, creep and so on of damaging behaviors under long-term service conditions (Ref 2). So, it is necessary to regularly test and analyze the performance (especially mechanical performance) of the preset structural materials and components in the reactors to ensure the safe operation of nuclear power facilities (Ref 3, 4). Due to the serious secondary radioactivity of materials caused by high flux neutron irradiation, the preparation and testing of all material standard samples must be completed in a hot cell, so the performance evaluation and development of structural materials in nuclear energy systems take a lot of time with high cost (Ref 2, 4). From the perspective of reducing the number of radioactive samples and improving the irradiation efficiency (the irradiation space is limited) of materials in the reactors (a hot cell is not needed, which reduces a lot of costs), and considering the simulated irradiation depth outside the reactors (neutron irradiation effect is simulated by heavy ions to shorten the evaluation period of irradiation), it is more effective to replace the American Society of Testing Materials (ASTM) and American Society of Mechanical Engineers (ASME) standard specification samples with smaller or even miniature samples. Therefore, the designs, mechanical tests and analysis techniques of miniature samples as well as the structure–activity relationships between the test results of miniature samples and the results of standard samples are important contents of the research and development of nuclear materials in recent years (Ref 3, 5).

Nondestructive testing techniques have played more and more important roles in getting the mechanical properties and damage degrees of equipment (Ref 6-9). The small punch test (SPT) is one of the nondestructive mechanical testing technologies developed in Europe, America and Japan in the 1980s (Ref 5-8), which uses miniature specimens of 10×10 mm square or disks with the diameter of 10, 8 or even 3 mm. In fact, 3-mm disks are now widely used and accepted as SPT means, because the size of this specification just matches the test samples of transmission electron microscope (TEM). Compared with the traditional mechanical test methods, SPT reduces the size of the test samples, which has great advantages and broad application prospects for material research in space, nuclear plants and other extreme environments (Ref 10-15).

SPT technology has been widely used to characterize the tensile properties, the ductile-brittle transition temperature

Zhaoyi Cheng, Jianrong Sun, and **Linqi Zhang**, Institute of Modern Physics, Chinese Academy of Sciences, Lanzhou 730000, China; and School of Nuclear Science and Technology, University of Chinese Academy of Sciences, Beijing 100049, China; and **Pengfei Tai** and **Hailong Chang**, Institute of Modern Physics, Chinese Academy of Sciences, Lanzhou 730000, China; **Yuting Wei**, School of Nuclear Science and Technology, Lanzhou University, Lanzhou 730000, China; **Rebecca Thuku**, School of Life Science, University of Chinese Academy of Sciences, Beijing 100049, China; and **Kelvin M. Gichuhi**, College of Engineering and Technology, Jomo Kenyatta University of Agriculture and Technology, Nairobi 00200, Kenya. Contact e-mail: sunjr@impcas.ac.cn.

(DBTT), the fracture toughness (J_{IC}), the creep damage characteristics, the fatigue properties, etc., which are aimed at various materials, such as steels, alloys and ceramics (Ref 6-34). Bruchhausen et al. (Ref 14) found that tensile properties such as yield strength (σ_y) and ultimate strength (σ_{UTS}) of P91 material could be obtained by load–displacement curves of SPT experiments. Jia and Dai et al. through the experiments of SPT discovered that the DBTT of F82H, T91 and Optimax-A steels increased a lot with the increasing radiation dose (Ref 22, 23). Mao et al. investigated 2.25Cr-1Mo steel fracture toughness (J_{IC}) of radiation, and they found the results of fracture toughness (J_{IC}) obtained from SPT with 3-mm diameter specimens were almost linear with the fracture strain (Ref 11, 13). Zhao and Song et al. analyzed the creep damage characteristics of Sanicro25 austenitic stainless steel and P92 steel by using SPT experiments and finite element modeling (FEM) simulations, and they discovered that the experimental creep curves in small punch creep (SPC) tests were similar to that in uniaxial creep (UC) tests (Ref 27-29). Lancaster et al. studied fatigue properties of the aerospace titanium alloy Ti-6Al-4V and the nickel-based superalloy C263 by using small punch fatigue (SPF) tests, and their results were consistent with uniaxial fatigue (UF) tests (Ref 6). Simonovski, Gao and Xue et al. evaluated the accuracy of some physical models with the combination of SPT experiments and FEM simulations (Ref 32-34). Simonovskid et al. found that Gurson–Tvergaard–Needleman (GTN) damage model can well predict the formation of cracks under the cold working conditions of 15-15Ti24CW and 15-15Ti46CW (Ref 32), Gao et al. predicted the fracture behavior of AA7075 aluminum alloy during hot forming by GTN damage model (Ref 33), and Xue et al. calculated the mechanical properties of materials by inverting the Johnson–Cook constitutive model parameters of materials (Ref 34).

However, due to the inhomogeneity of stress and deformation conditions, the main difficulty of SPT experiments is that it is not as easy to obtain the relevant materials parameters as easily as the standard test methods (Ref 10-12). Therefore, there is still no generally accepted program for getting basic materials properties from SPT experimental data (Ref 7, 10-12). The most difficult thing is that the correlation between each researcher's conclusions has not been established, which leads to the fact that the researchers still need to carry out a large number of standard experiments to compare with the experimental data obtained from SPT. Also, there are still some problems in SPT technology, such as the lack of normalization methods for miniature sample data and the size effect of miniature samples (Ref 10, 35-37). At present, researchers recognize that these problems can be solved by comparing the SPT experimental results with the simulative results calculated by using advanced materials models, so as to obtain the relationships between the data (Ref 10-12). In addition, there are some limitations in the use of the SPT method for the characterization of engineering mechanical properties of materials with significant mechanical anisotropy (e.g., Zr alloys with significant plastic anisotropy). The greatest source of this limitation is the size effect of miniature specimens. The thickness of miniature specimens is only dozens or hundreds μm (only a few grains size), which makes the proportion of the anisotropy of the grain orientation and the lattice itself more significant. Furthermore, the other side comes from the imprecision of the theoretical model. For example, the error in calculating the fracture toughness of each metallic material by the maximum fracture energy density may be relatively large; and whether it is used for other materials needs to be further verified. However, it is generally assumed that the above limitations can be ignored. On the one hand, the difference between the values of the SPT method and the standard test is relatively small. On the other hands, when materials with significant anisotropy are tested by using the SPT method, the results are all labeled as performance values in one direction, and there is no possibility of misinterpretation. Therefore, in terms of the scope of use of the SPT method, it is a test method with universal applicability.

In this paper, a comparative study is conducted on the SPT experiments, the miniature specimens tensile test experiments and the FEM simulations of SPT based on the miniature specimens' tensile test results verify and establish the elastic–plastic parameters of materials obtained by the SPT method. Moreover, a new comparison scheme is also provided for obtaining accurate data from SPT experiments of miniature specimens. By establishing constitutive relations, SPT will save a great deal of workforce and financial resources for the evaluation of mechanical properties for nuclear material, and at the same time, it will also lay the foundation for establishing the relevant program for obtaining basic materials properties from SPT experimental data. Based on these, merely after SPT experiments, the almost complete mechanical properties of materials can be reasonably and accurately obtained in the future, such as elastic modulus (E), fracture toughness (J_{IC}), fracture energy, yield strength (σ_y) and ultimate strength (σ_{UTS}).

SIMP steel is a type of reduced-activation ferritic/martensitic (RAFM) steels cooperatively developed by the Institute of Modern Physics (IMP) and the Institute of Metal Research (IMR), Chinese Academy of Sciences (CAS) as the structural materials for China initiative Accelerator Driven sub-critical System (CiADS) (Ref 38, 39). Because of its high silicon (Si) concentration, the resistance to liquid metal corrosion of SIMP steel is further improved as well as its resistance to irradiation swelling than T91 steel, and a large number of SIMP steel experiments about irradiation, corrosion and mechanical tests are being carried out (Ref 39-41).

2. Experimental

2.1 Materials and Specimens

The steel materials studied in this paper were from the 5-ton levels SIMP steel forged by the Institute of Metal Research, Chinese Academy of Sciences. Detailed chemical compositions of SIMP steel are presented in Table 1, and the steel was used in the normalized and tempered condition, as noted (Ref 38-41). Microspecimens (tensile test and SPT specimens) were fabricated via low-speed unidirectional wire electrical discharge machining (WEDM-LS). Firstly, the surfaces of the samples were mechanically polished with sandpaper with various degrees of roughness, and secondly, they were fine mirror polished with a diamond spray of 0.5 μm. Finally, all the samples were cleaned by ultrasonic waves in acetone. The design of miniature tensile test specimens is shown in Fig. 1(a), and the microsamples used for SPT are in the form of disks with a diameter of 3 mm and a thickness of 0.1, 0.2 and 0.3 mm. Besides, the dimensions of the above samples meet standards specified in detail in the EUCoP (Ref 42, 43).

Table 1 The nominal composition of SIMP steel in wt.%

Material	C	Si	Cr	Mn	W	Ta	V	S	P	Fe
SIMP	0.22	1.22	10.24	0.52	1.45	0.12	0.18	0.0043	0.004	Bal.

Normalization: 1050 °C, 30 min; temperature: 760 °C, 90 min.

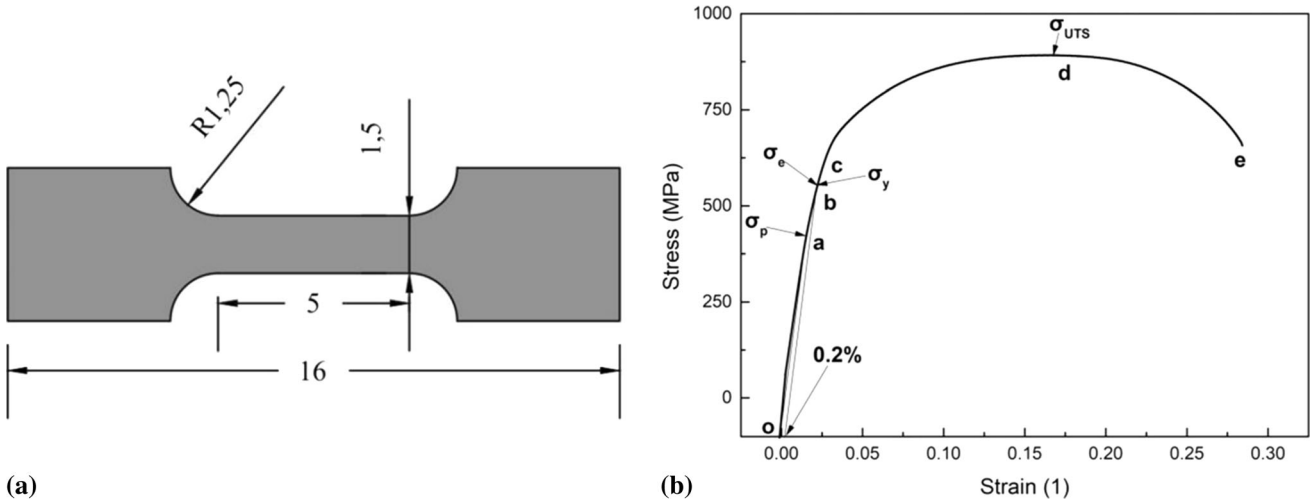

Fig. 1 Tensile experiments. (a) Dimensions (mm) of the small tensile specimen of SIMP steel and (b) engineering tensile stress–strain curve measured at RT of SIMP steel (1 represents the strain unit of 1 mm/mm)

2.2 Tensile Tests

To obtain the properties (elastic–plastic parameters) of SIMP steel, a 20-kN MTS machine was used to carry out uniaxial tensile tests on miniature tensile test specimens (Ref 37, 44, 45). The tensile tests were performed at a constant speed of 0.3 mm/min corresponding to a nominal strain rate of 1.0×10^{-3} s^{-1}, and the samples of five thicknesses (0.25, 0.30, 0.45, 0.50 and 0.65 mm) were tested four times for each. The typical nominal stress–strain (engineering tensile stress–strain) curve of the SIMP steel specimens was tested at room temperature (RT), which is illustrated in Fig. 1(b). The relationships between nominal stress (σ) and nominal strain (ε) as follows (Ref 15, 31):

$$\sigma = \begin{cases} E\varepsilon & \varepsilon \le \sigma_p/E \\ \sigma_e & 0 \le \varepsilon_p \le 0.2\% \\ \sigma_y & 0.2\% < \varepsilon_p < \varepsilon_L \\ \alpha\varepsilon_p^n & \varepsilon_L < \varepsilon_p < \varepsilon_2 \\ \sigma_B & \varepsilon_p > \varepsilon_2 \end{cases} \quad \text{(Eq 1)}$$

where σ_p is the ultimate proportional strength, σ_e is the ultimate elastic strength, σ_y is the yield strength, σ_{UTS} is the ultimate strength, and the corresponding values are also shown in Fig. 1(b). The elastic phase is the o–b segment, and the engineering stress should be in direct proportion to the engineering strain in the o–a segment. Although engineering stress is not strictly proportional to the engineering strain of the a–b segment, the tensile deformation will disappear if unloaded. Therefore, the elastic phase also includes the a–b segment corresponding to 0.2% plastic strain. The yield phase is the b-c segment, in which the material loses its ability to resist deformation, however, this phase does not exist in SIMP steel. The strengthening phase is the c–d segment, which restores resistance to deformation. The local necking phase is the d–e segment, where the samples appear necking phenomenon and are quickly fractured. Furthermore, the method is currently only applicable to the process of tensile testing of metallic materials.

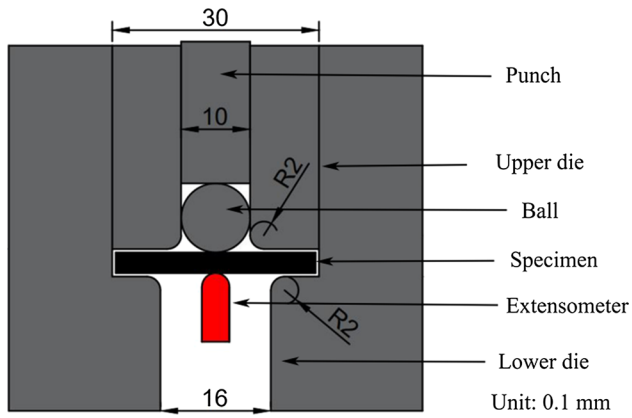

Fig. 2 A schematic diagram shows the set-up of SPT (unit: 0.1 mm)

2.3 Small Punch Tests (SPT)

SPT experiments were performed by using an improved hydraulic-driven MTS device (Ref 11-15, 27-31). The detailed schematic diagram of the SPT device is depicted as in Fig. 2. The device consists of a small punch, an upper die, a rigid ball with a diameter of 1 mm, a specimen, a lower die and an extensometer. In SPT experiments, the SIMP steel specimen

was clamped between the upper and lower dies. In addition, screws were fixed between the upper and lower dies to ensure that the specimen was always clamped. The SPT experiments were carried out at a constant speed of 0.2 mm/min (Ref 11-17). Here, 3-mm diameter disk miniature specimens were used to test SIMP steel specimens of three thicknesses (0.1, 0.2, and 0.3 mm) at RT (Ref 42, 43), with six repetitions of each thickness.

The typical load–displacement curve of SPT experiments for SIMP steel and distributions of the shear stress of cross section (x–y plane) across the specimens of FEM simulations is illustrated in Fig. 3. The load–displacement curve includes (I) elastic bending, (II) plastic bending, (III) plastic membrane stretching and (IV) plastic instability, and it corresponds to (a), (b), (c) and (d) of the shear stress distribution diagram, respectively. Moreover, the elastic–plastic transition force (F_e), the maximum force (F_m) and the fitted straight line $F(u)$ are shown in Fig. 3.

2.4 Finite Element Modeling (FEM)

The ABAQUS 6.14-1 standard code was used for FEM (Ref 16-20). The details of FEM simulations used for SPT are depicted as in Fig. 4. The physical model is composed of a central axis, a punch indenter with a diameter of 1 mm, an upper die, a disk specimen, and a lower die is presented in Fig. 4(a). A friction coefficient of 0.2 was set between the surfaces of the upper and lower dies in contact with the specimen in order to prevent the disk specimen from sliding, as the results of Kumar and Simonovski et al. studies agreed that the fitting degree between simulation results and experiment results is the highest when the friction coefficient is 0.2 (Ref 19, 30). In the current work, the modeling does not take into account a damage model. In addition, the displacement and angle were completely fixed on the lower die, and a force of 440 N that can only go down was set on the upper die, which were the boundary conditions (Ref 19, 30). Furthermore, there are two loading methods in FEM calculations, i.e., force loading and displacement loading. In this paper, the displacement loading at a steady velocity of 0.2 mm/min was used to simulate SIMP steel with three thicknesses (0.1, 0.2 and 0.3 mm) is illustrated in Fig. 4(b). The 6854 axisymmetric linear reduction integral elements (CAX4R) were used to simulate the disk samples are shown in Fig. 4(c). In addition, the fine meshes were divided around the disk sample about 1/3 of the area. The size of the fine meshes divided by ABAQUS software was 0.02, and the size of the coarse meshes was 0.1. Here, the fine mesh optimization was adopted to improve the accuracy of the calculations. Finally, the material properties (elastic modulus, Poisson's ratio and the true stress–plastic strain) of miniature tensile test specimens as the initial parameters were utilized to perform FEM simulations of SPT at RT.

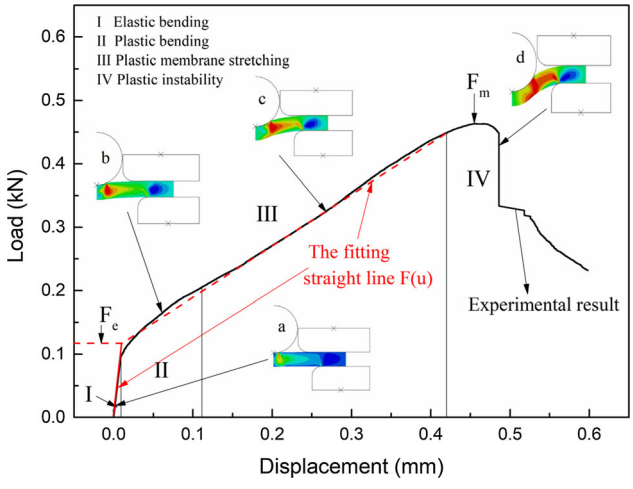

Fig. 3 The typical load–displacement curve of SPT experiments for SIMP steel and distributions of the shear stress of cross section (x–y plane) across the specimens of FEM simulations for (a) elastic bending, (b) plastic bending, (c) plastic membrane stretching and (d) plastic instability

2.5 Morphology and Microstructure Characterization

After the SPT experiments, SIMP steel specimens were cleaned by ultrasonic alcohol and then air-dried on a quick qualitative filter paper. These specimens were prepared for morphology and microstructure characterization. The morphology and microstructure of three thicknesses SIMP steel specimens were collected by ultra-high-resolution field emission scanning electron microscopy (HRSEM), which was carried out with a SU8020 instrument (HITACHI, Japan) equipped with the energy disperse spectroscopy (Octane Plus) detector (EDAX, AMETEK, the USA). The electron gun of HRSEM is a cold field emission source, which was operated at the standard mode with an accelerating voltage of 5.00 kV. After adjustment and comparison of various magnification multiples, four magnification multiples of 100, 5000, 40000 and 80000 times were finally selected for characterization.

3. Results

3.1 Tensile Properties of SIMP Steel

The nominal stress–strain curves of SIMP steel with different thicknesses are obtained by tensile tests of miniature samples at RT as shown in Fig. 5(a). The results show that the nominal stress–strain curves of SIMP steel with thicknesses of 0.30, 0.45, 0.50 and 0.65 mm are approximately the same in the elastic and plastic phases (the errors are less than 2.5%), and the results are similar to those obtained by the tensile tests of standard size samples (Ref 39). However, when the thickness is 0.25 mm, the result is obviously different. It is estimated that when the thickness is 0.25 mm, the size effect should be taken into account in the tensile test result of miniature samples. The grain size of the SIMP steel is about 110 μm. When the thickness of the micro-tensile samples is reduced to a few grains, the size effect is significantly enhanced, so that the tensile test results are remarkably increased and more dispersed. The above phenomenon can be perfectly fitted and explained by the strain gradient plasticity theory based on the dislocation mechanism developed by Nix and Gao (Ref 46, 47). The normalized nominal (black) stress–strain curve and true (red) stress–strain curve of SIMP steel by miniature specimens tensile tests are illustrated in Fig. 5(b). The relationships among nominal stress (σ), nominal strain (ε), true stress (σ_{true}) and true strain ($\varepsilon_{\text{true}}$) as follows:

$$\varepsilon_{\text{true}} = \int \mathrm{d}\varepsilon_{\text{true}} = \int_{L_0}^{L} \frac{\mathrm{d}L}{L} = \ln\left(\frac{L}{L_0}\right) = \ln(1+\varepsilon) \qquad \text{(Eq 2)}$$

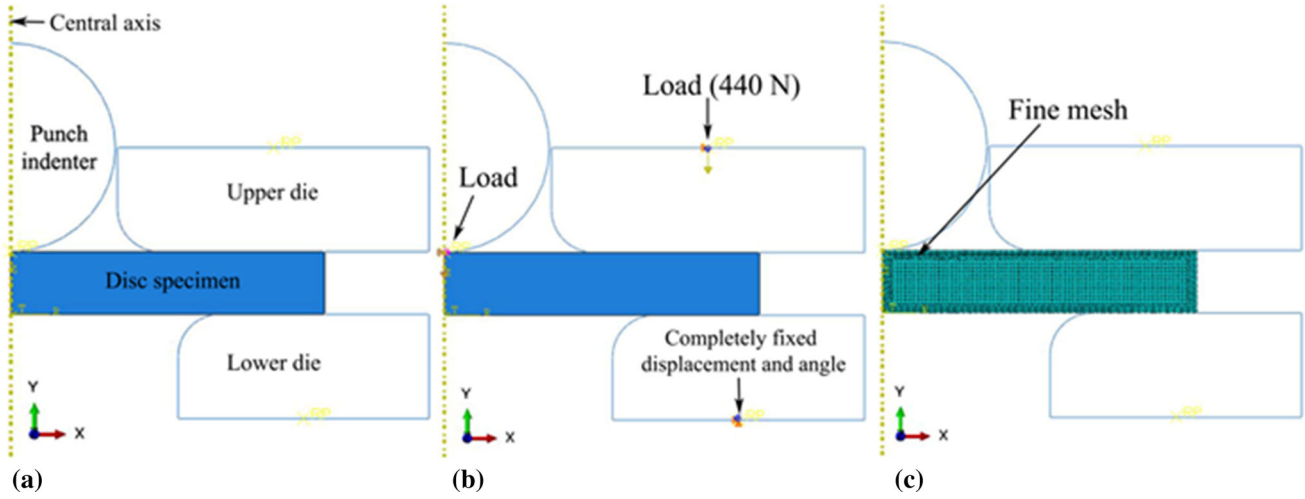

Fig. 4 Finite element analysis model used for SPT. (a) Physical model, (b) the boundary conditions and (c) the corresponding mesh structure

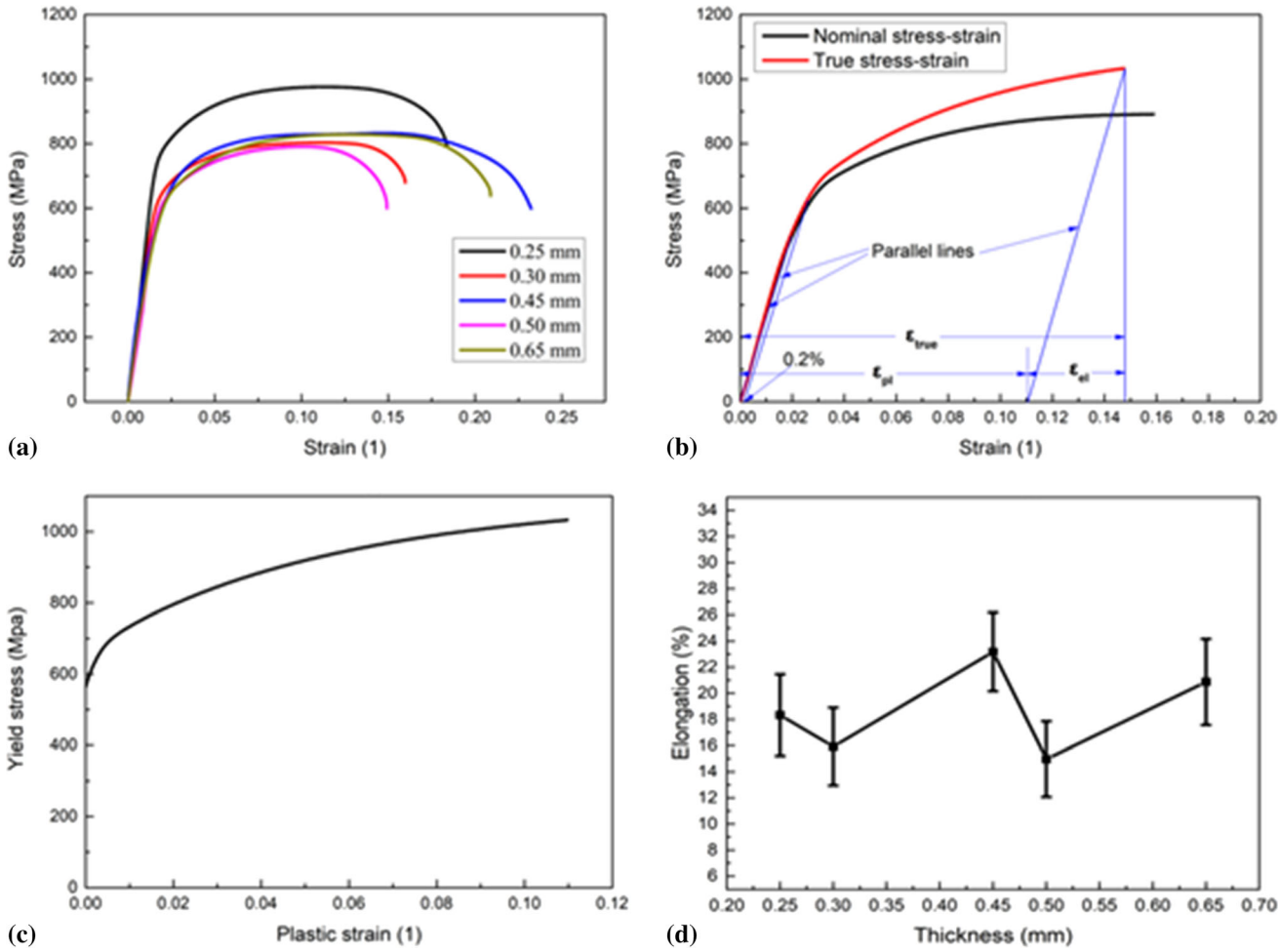

Fig. 5 (a) Nominal tensile stress–strain curves measured at RT of five thicknesses (0.25, 0.30, 0.45, 0.50 and 0.65 mm) SIMP steel, (b) normalize nominal (black) stress–strain curve and true (red) stress–strain curve of 0.30-mm thickness SIMP steel, (c) The stress–plastic strain curve of 0.3-mm thickness SIMP steel and (d) the elongation at fracture (%) (Color figure online)

$$\sigma_{\text{true}} = \frac{F}{A} = \frac{FL}{A_0 L_0} = \sigma(1+\varepsilon) \qquad \text{(Eq 3)}$$

Finally, as presented in Fig. 5(c), the true stress–plastic strain curve is obtained by using the true stress–strain curve, and the true stress–plastic strain curve is taken as SIMP steel

properties to input for the FEM simulations. The formulas among ε_{pl}, σ_{true}, E, $\varepsilon_{\text{true}}$, ε_{el}, σ_y, ε_y, σ_p and ε_p as below:

$$E = \frac{\sigma_p}{\varepsilon_p} = \frac{\sigma_y}{\varepsilon_y - 0.002} \quad \text{(Eq 4)}$$

$$\varepsilon_{pl} = \varepsilon_{\text{true}} - \varepsilon_{el} = \varepsilon_{\text{true}} - \frac{\sigma_{\text{true}}}{E} \quad \text{(Eq 5)}$$

where ε_{pl} is the true plastic strain, $\varepsilon_{\text{true}}$ is the true strain, ε_{el} is the true elastic strain, and the relative values are depicted as in Fig. 5(b). In addition, the elongation at fracture of tensile test for SIMP steel is shown in Fig. 5(d). The elongation at fracture has little change under five thicknesses, ranging from 15 to 25% basically.

3.2 SPT Experiments and FEM Simulations of SIMP Steel

The results of small punch load–displacement curves for different thicknesses (0.1, 0.2 and 0.3 mm) SIMP steel by experiments and calculations at RT are presented in Fig. 6. There is virtually no difference in the results calculated by FEM compared with the SPT experimental results, and they just do not perfectly fit in the plastic instability stage. The elastic–plastic transition force (F_e) and the maximum force (F_m) increase obviously with the thickness of specimens as shown in Fig. 6(a) and (b); however, Fig. 6(a) presents that the displacement of the fracture position does not increase with the thickness of SIMP steel. As illustrated in Fig. 6(b), the results of F_e and F_m obtained by experiments and calculations are roughly equal. Moreover, the errors of the elastic–plastic transition force (F_e) obtained by experiments and calculations are 7.95%, 8.82% and 1.33% on the specimens with different thicknesses (0.1, 0.2 and 0.3 mm) severally. Further, the errors of the maximum force (F_m) obtained by experiments and calculations are slightly larger, and then, they are 5.57, 17.70 and 18.09%, respectively.

3.3 Application to R_{mc}, R_{eHc} and $R_{tc0.5}$

The parameters of the compression strength (R_{mc}), the upper compression yield strength (R_{eHc}) and the proof strength-total compression ($R_{tc0.5}$) are all obtained directly from the SPT experiments, which are very important for analyzing the properties of the material. Similar to the ultimate elastic strength (σ_e) is equal to the yield strength (σ_y) in the engineering stress–strain curve is shown in Fig. 1(b), the compression strength (R_{mc}) in the experimental values of SPT experiments is equal to the upper compression yield strength (R_{eHc}). For determining the compression strength, the upper compression yield strength and the proof strength-total compression of the SIMP steel from the SPT empirical correlations between the material properties and the characteristics pointed on the load–displacement curves are used (Ref 14, 21, 42, 43):

$$R_{mc} = R_{eHc} = \alpha_1 \frac{F_m}{h_o^2} + \alpha_2 \quad \text{(Eq 6)}$$

$$R_{tc0.5} = \beta_1 \frac{F_e}{h_o^2} + \beta_2 \quad \text{(Eq 7)}$$

where α_1, α_2, β_1 and β_2 are a constant, respectively. F_e is the elastic–plastic transition force, F_m is the maximum force, and h_o is the sample thickness in the SPT experiments. The distribution of the compression strength (R_{mc}) and the upper compression yield strength (R_{eHc}) along with F_m/h_o^2 are provided in Fig. 7. The result of the linear fitting is $y = -0.0058x + 100.56$, and the correlation index (R^2) is 0.9894. Similarly, the distribution of the proof strength-total compression ($R_{tc0.5}$) along with F_e/h_o^2 is depicted as in Fig. 8. The result of the linear fitting is $y = 0.0327x - 19.375$, and the correlation index (R^2) is 0.9408. It is not difficult to discover that the fitting degrees of the above two unary polynomial regression equations both are relatively high because the correlation indexes are greater than 0.94. Besides, the detailed factors according to Eq 6 and 7 obtained by the linear fitting are presented in Table 2.

3.4 The Comparisons of FEM Simulations and SEM Observations

The shear stress is the main cause that leads to the fracture properties of SIMP steel specimens in SPT experiments, so it is particularly important to analyze the distribution of shear stress in FEM simulations. The detailed distribution of shear stress contour plot of 0.3-mm-thickness SIMP steel calculated by FEM is shown in Fig. 9. The S represents the shear stress, and

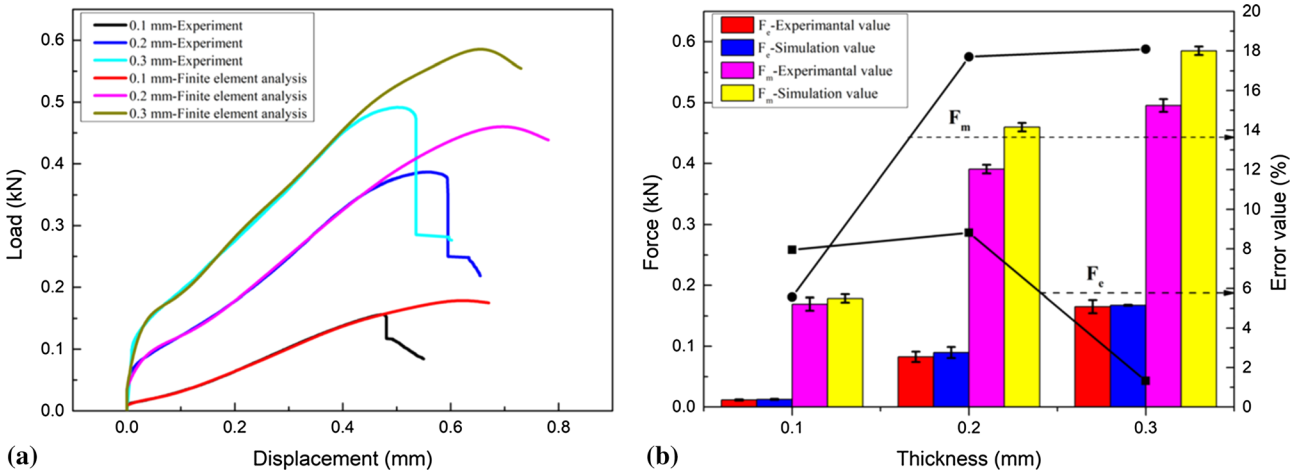

Fig. 6 (a) Experimental and simulation results of SPT load–displacement curves for 0.1-, 0.2- and 0.3-mm thickness SIMP steel at RT and (b) detailed results of F_e, F_m obtained by experiments and simulations as well as the errors of experiments and simulations values

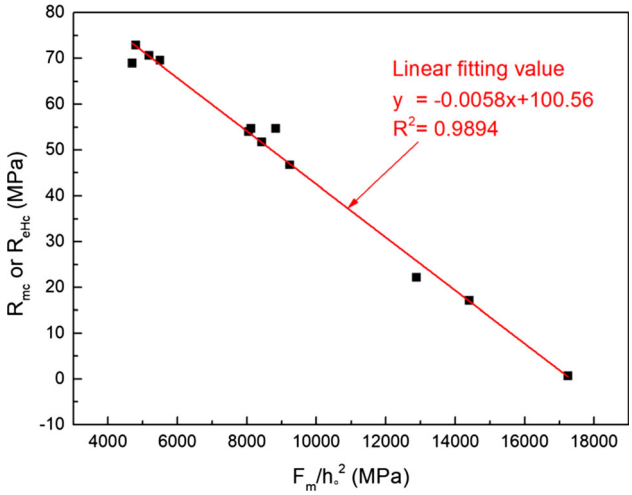

Fig. 7 Distribution of the compression strength (R_{mc}) and the upper compression yield strength (R_{eHc}) along with F_m/h_o^2

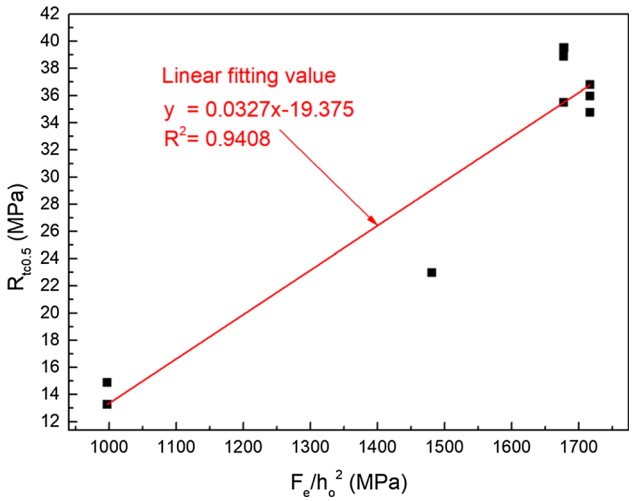

Fig. 8 Distribution of the proof strength-total compression ($R_{tc0.5}$) along with F_e/h_o^2

Table 2 The factors according to Eq 6 and 7 from the linear fitting value

Factor	α_1	α_2	β_1	β_2
Linear fitting value	− 0.0058	100.56	0.0327	− 19.375

S12 represents the shear stress of the *X*–*Y* plane of the two-dimensional plane, and then, S12 specifically refers to shear stress in this paper. In Fig. 9, the maximum shear stress is connected into an arc line, which is consistent with the arc line observed by SEM for the sample in SPT experiments. The distribution of shear stress differs markedly with respect to the upper and lower surfaces. Further, the distance between the maximum shear stress on the upper surface and the center of the sample is obviously greater than that on the lower surface.

To prove the rationality and accuracy of FEM simulations, the FEM simulation results are compared with the SEM observation results. The distribution of shear stress with the distance from the center of the sample on the upper and lower surfaces of 0.3-mm-thickness SIMP steel is illustrated in Fig. 10(a). The detailed result of amplification 100 times for the SPT experiments 0.3-mm-thickness sample by SEM is shown in Fig. 10(b). In Fig. 10(a), the distance between the maximum shear stress and the sample center is 0.424 mm on the upper surface and 0.406 mm on the lower surface. Also, in Fig. 10(b), the distance between the fracture and the sample center is 0.412 mm on the upper surface and 0.399 mm on the lower surface. As can be easily found, the distances between the maximum shear stress and the 0.3 mm thickness specimen center on the upper and lower surfaces by FEM calculations are almost equivalent to the distances between the fracture and the 0.3-mm-thickness specimen center by SEM observations.

As presented in Table 3, the radial distance from the three thicknesses (0.1, 0.2 and 0.3 mm) SIMP steel fracture to the center of the specimen at the upper surface and lower surface by FEM and SEM. It can be shown obviously that the radial distances from the SIMP steel fracture to the center of the specimens at the upper surface and lower surface by FEM and SEM increase with the thickness. Furthermore, except for the lower surface of the 0.2-mm-thickness SIMP steel sample, all radial distances from fracture to the center of the samples by FEM simulations are slightly bigger than that by SEM observations. Especially important, all errors between the FEM calculations results and the SEM observations results are less than 5%, even less than 3.2%.

3.5 Fracture Energy (SP Energy) of SIMP Steel

The fracture energy is the energy needed for the crack propagation per unit area of material under load, and it is an important physical quantity for the experiments of SPT. For the sake of further proving the rationality and accuracy of FEM simulations applied to SPT experiments, the fracture energy obtained by SPT experiments and FEM simulations is compared. The detailed schematic diagram of fracture energy (SP energy) calculated for SPT is depicted as in Fig. 11. The formulas of fracture energy and the maximum force are calculated as follows (Ref 14, 24, 25, 31):

$$W_t = v\int_0^{\varepsilon_0}\sigma \mathrm{d}\varepsilon = \int_0^{u_0} P(u)\mathrm{d}u \qquad \text{(Eq 8)}$$

$$P_m = \Delta P_{eb} + \Delta P_{pb} + \Delta P_{\mathrm{pms}} + \Delta P_{pi} \qquad \text{(Eq 9)}$$

Here, W_t is the fracture energy, v is the volume of the miniature sample fracture section, σ is the stress, ε is the strain, ε_0 is the strain at the moment when the sample is greatly fractured, $P(u)$ is the load, u is the displacement, u_0 is the value of the corresponding pressing displacement at the moment when the sample is greatly fractured, P_m is the maximum force, as well as ΔP_{eb}, ΔP_{pb} and ΔP_{pms} together with the sum total of about 80% of the P_m.

It can be seen that the fracture energy results calculated by the FEM simulations are basically on a par with those obtained by the SPT experiments from Fig. 12. The fracture energy rises with the SIMP steel specimen thickness by SPT experiments and FEM calculations, in which the corresponding relationship is not linear. Moreover, the standard deviations of fracture energy calculated by FEM under different thicknesses are less than the standard deviations of SPT experimental fracture

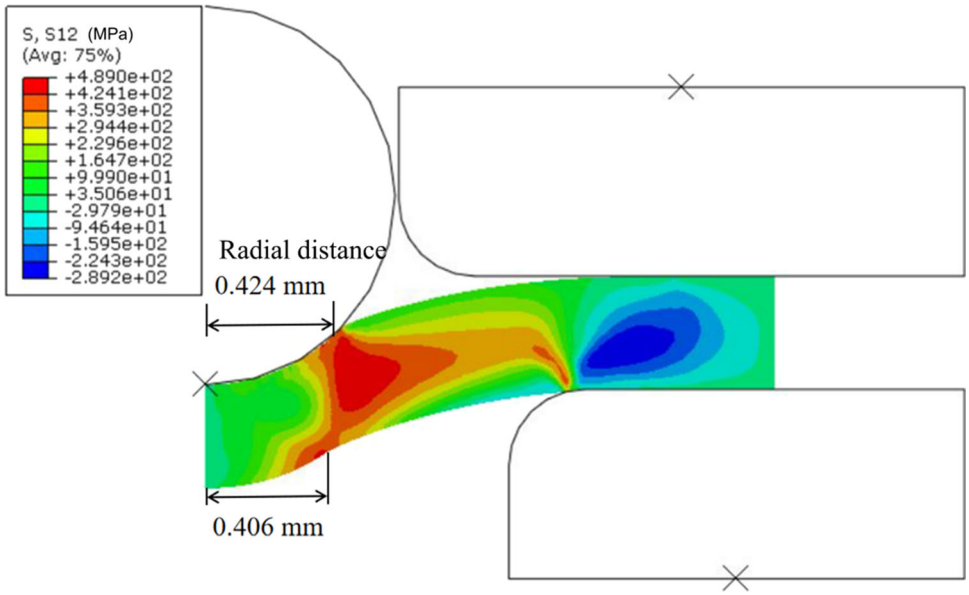

Figure 9. Distribution of the shear stress of cross section (X–Y plane) across the specimen for SIMP steel with the thickness of 0.3 mm by FEM. (S represents the shear stress, and S12 represents the shear stress of the X–Y plane of the two-dimensional plane, unit: MPa.)

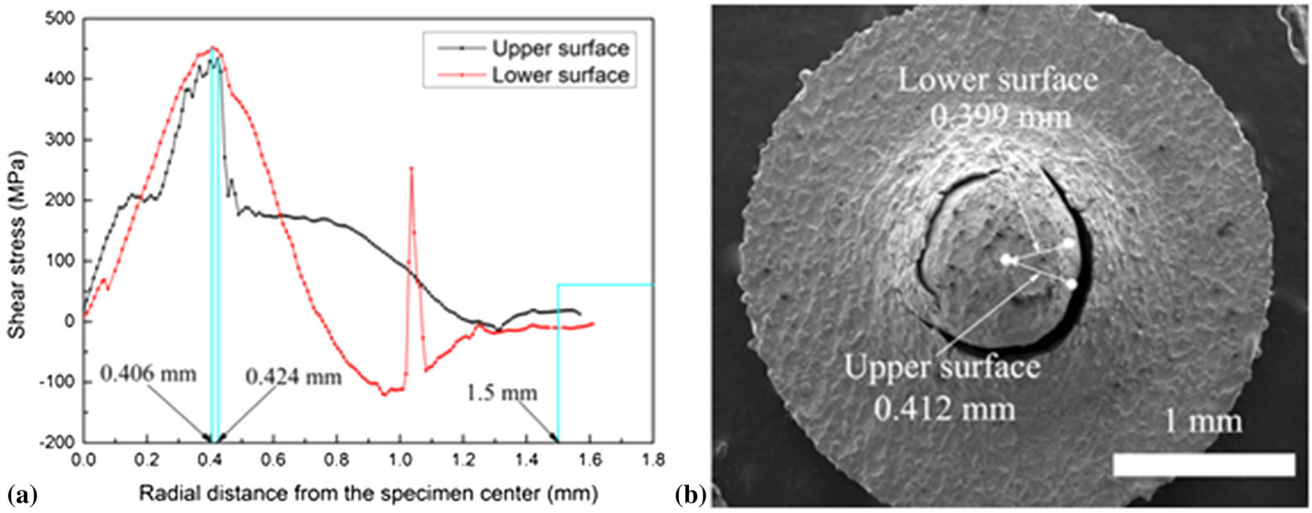

Fig. 10 (a) Development of the shear stress (S12) with the distance from the center of the sample on the upper and lower surfaces of the 0.3-mm thickness SIMP steel was simulated at RT during the deformation process and (b) SEM micrographs of a higher magnification showed the fracture surface of 0.3-mm thickness SIMP steel SPT experiments specimen

Table 3 The radial distances from the three thicknesses SIMP steel fracture to the center of the specimens at the upper surface and lower surface by FEM and SEM

Thickness, mm	Upper surface			Lower surface		
	FEM, mm	SEM, mm	$\frac{\text{SEM}-\text{FEM}}{\text{FEM}} \times 100\%$	FEM, mm	SEM, mm	$\frac{\text{SEM}-\text{FEM}}{\text{FEM}} \times 100\%$
0.1	0.328	0.319	0.0274	0.281	0.275	0.0214
0.2	0.384	0.380	0.0104	0.350	0.361	0.0314
0.3	0.424	0.412	0.0283	0.406	0.399	0.0173

energy, which are about half of the standard deviations of experimental fracture energy. Extremely important, the errors of calculations and experiments are inferior to 9% in SIMP steel samples of three thicknesses.

3.6 Distributions of Shear Stress for SIMP Steel by FEM

The shear stress calculation formula in the SPT experiments as follows (Ref 16, 26):

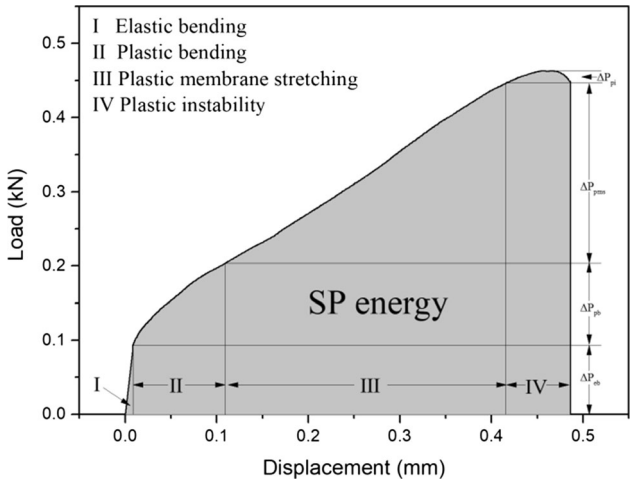

Fig. 11 Schematic diagram of fracture energy (SP energy) calculated for SPT

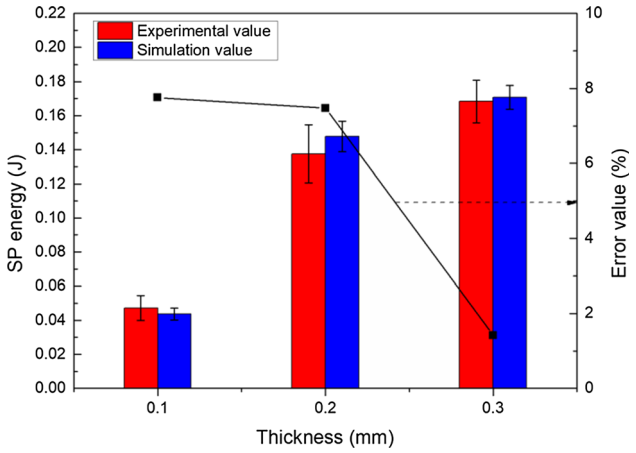

Fig. 12 Experimental and simulation results of SP energy for different thicknesses (0.1, 0.2 and 0.3 mm) SIMP steel at RT

$$S = \frac{F_s}{A} \quad \text{(Eq 10)}$$

F_s is the shear force, A is the shear plane area, S is the shear stress, and its direction is perpendicular to the normal stress direction. The shear stress distributions with the radial distances from the center of the specimens on the upper and lower surfaces are illustrated in Fig. 13. The distances between the maximum shear stress and the sample center increase with the increase in the sample's thickness are provided in Fig. 13(a), which corresponds to the results of the upper surface in Table 3. In a like manner, the distances between the maximum shear stress and the sample center also increase with the increase in the sample's thickness are depicted as in Fig. 13(b), which are consistent with the results of the lower surface in Table 3. In addition, the maximum distances from the sample center on the upper and lower surfaces are obviously larger than 1.5 mm at the fractured elongation section, which matches with the reflected processes of arc deformation in the SIMP steel samples observed by SEM as presented in Fig. 10(b) and 15. Nevertheless, the distributions of the shear stress with the distances from the center of the samples for the clamped section on the lower surface are more complicated than that on the upper surface.

The detailed distributions of the shear stress in the cross section (x–y plane) of the SIMP steel specimens obtained by FEM simulations are shown in Fig. 14. Here, the thicknesses of the samples from left to right are 0.1, 0.2 and 0.3 mm in turn, and the properties from top to bottom are elastic bending, plastic bending, plastic membrane stretching and plastic instability, respectively. There is the unrecoverable crosswise elongation in Fig. 14(c), (g) and (k), which corresponds to the fractured elongation section in Fig. 13. At the same time, Fig. 14 contains a large amount of information about the SPT, such as displacement, stress, strain and the state of deformation. Considerably important, the contour maps obtained by FEM simulations can accurately represent the whole processes of SPT experiments.

3.7 Details of SPT Experimental Fracture by SEM Observations

Figure 15 presents the fracture appearances of specimens for SPT experiments. As provided in Fig. 15, the thicknesses of the SIMP steel specimens from left to right are 0.1, 0.2 and 0.3 mm in sequence, and the magnification times from top to bottom are 100, 5000, 40000 and 80000 times severally (Ref 17, 22, 23, 25-29). From the microscopic results, it can be seen that SIMP steel is a polycrystalline material, and its fracture belongs to the dimple fracture, and dimples grow and connect with each other through the formation of hollows in the process of the SPT experiments. It is well known that the size, depth, distribution, shape and density of dimples directly affect the material properties of ductility and stress state. As can be clearly seen from the diagrams in Fig. 15, the size, depth and density of dimples become larger and more uniform with the increase in SIMP steel sample thickness. Roughly speaking, these show that the elongation, hardness and stress state of SIMP steel become all the better with increasing thickness. Moreover, the material properties obtained from the dimple parameters of samples with different thicknesses are consistent with the results of FEM simulations, and the detailed parameters of dimples of SIMP steel at the enlargement factor of 80000 times are sketched in Table 4.

4. Discussion

Initially, miniature tensile samples of SIMP steel with five thicknesses were tested, and the engineering stress–strain curves obtained are roughly consistent with the experimental results obtained by Liu et al. using standard samples (Ref 39). Simultaneously, considering the size effect proposed by Simons et al. in the miniature samples tensile tests (Ref 36), the thickness limit of the size effect is 0.25 mm at miniature samples with a total length of 16 mm. Furthermore, a series of transformation formulas are used to obtain the material properties required for FEM calculations as shown in Fig. 5. Finally, using the above properties of SIMP steel as initial input parameters, the load–displacement curves are calculated by FEM simulations. It is obvious that the results obtained from FEM simulations are identical to the SPT experimental results as illustrated in Fig. 6.

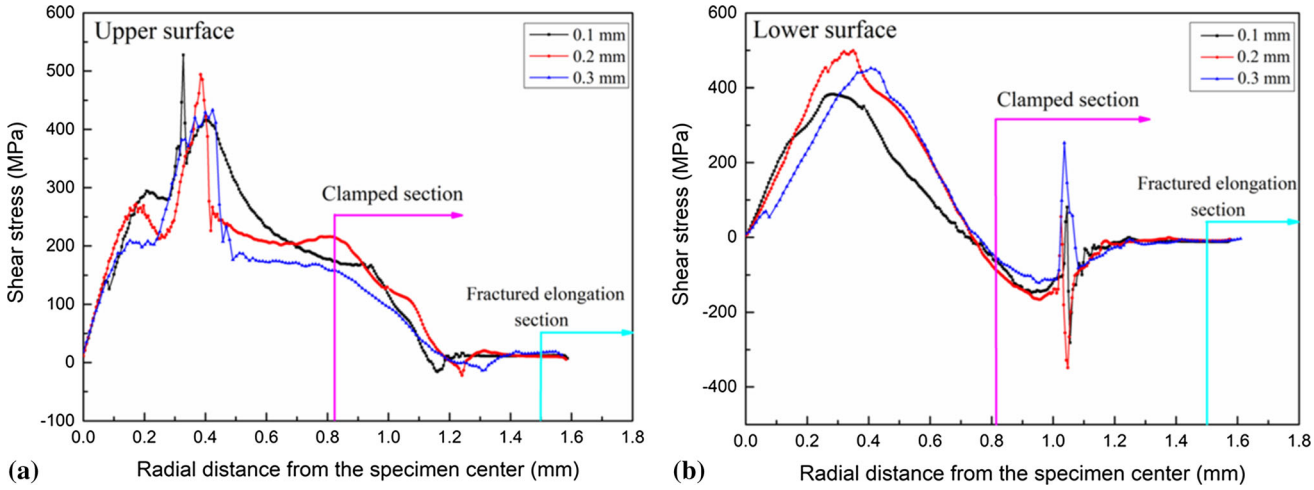

Fig. 13 Developments of shear stress (S12) with final state of deformation in three thicknesses (0.1, 0.2 and 0.3 mm) SIMP steel simulated at RT. (a) Upper surface and (b) lower surface

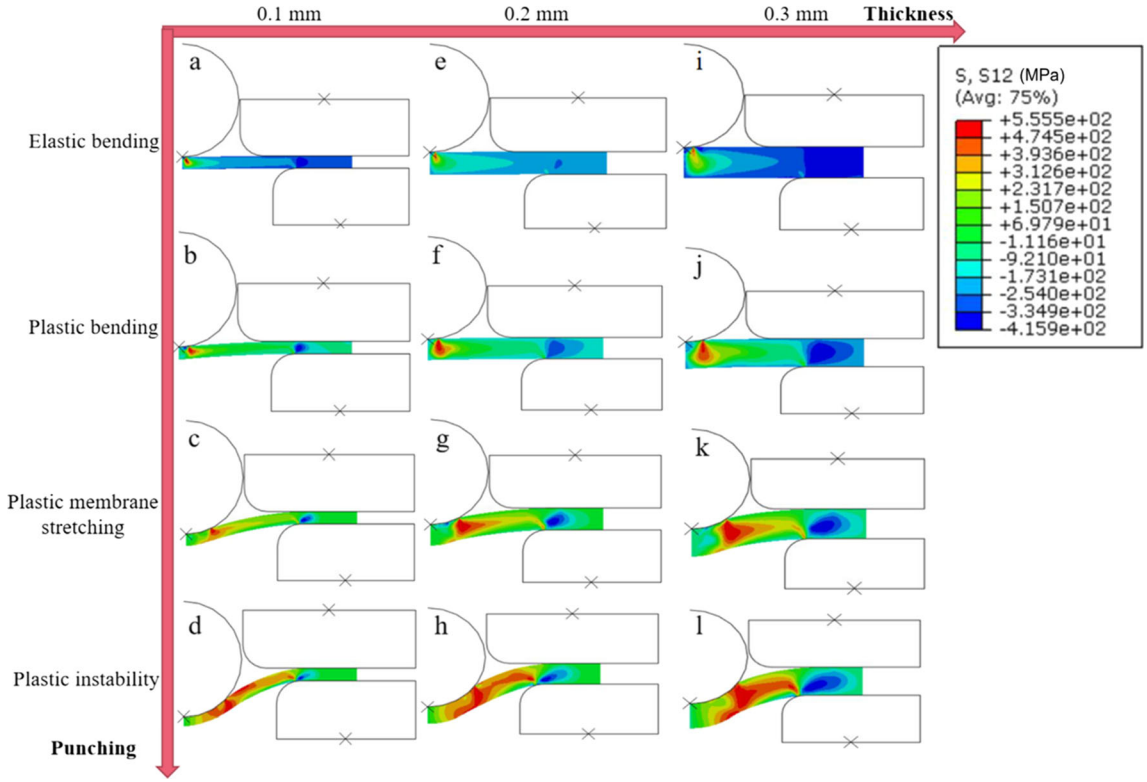

Fig. 14 Distributions of the shear stress for cross section (*X*–*Y* plane) across the SIMP steel specimens by FEM (the thicknesses of the samples from left to right are 0.1, 0.2 and 0.3 mm in turn, and the properties from top to bottom are elastic bending, plastic bending, plastic membrane stretching and plastic instability, respectively. (S represents the shear stress, and S12 represents the shear stress of the *X*–*Y* plane of the two-dimensional plane, unit: MPa)

The FEM simulation results obtained by using the material properties from the standard tensile samples are consistent with the experimental results of the SPT (Ref 20). More specifically, using the properties of SIMP steel obtained by using the micro-tensile samples as initial input parameters of FEM, the load–displacement curves are calculated by FEM simulations, and the results are identical to the SPT experimental results as illustrated in Fig. 6. This indicates that the complete material properties of the standard tensile tests can be obtained by merely conducting SPT experiments. The tensile yield strength (σ_y) and ultimate strength (σ_{UTS}) of the materials are successfully predicted by using F_e and F_m obtained from the load–displacement curves in the SPT experiments (Ref 14, 21, 42, 43). Further on, the experimental results indicate that the compression strength (R_{mc}), the upper compression yield strength (R_{eHc}) and the proof strength-total compression ($R_{tc0.5}$) directly from SPT experiments can also be obtained by F_e and F_m as presented in Fig. 7 and 8 and Table 2.

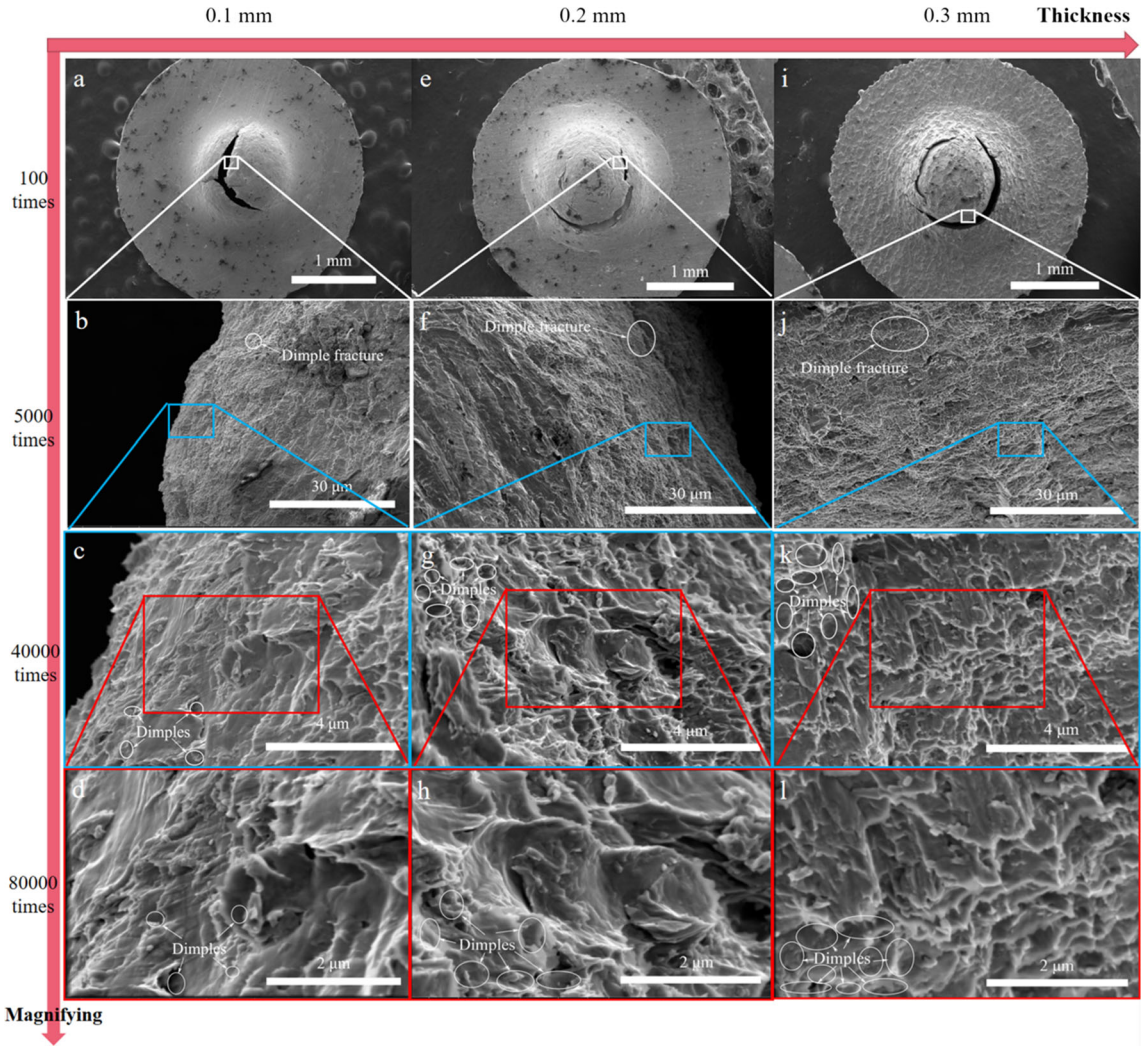

Fig. 15 SEM micrographs of a higher magnification show the fracture surfaces of SIMP steel specimens for SPT experiments. (the thicknesses of the SIMP steel specimens from left to right are 0.1, 0.2 and 0.3 mm in sequence, and the magnification times from top to bottom are 100, 5000, 40000 and 80000 times severally.) A few typical dimples for labeling are signed at high-resolution pictures.

Table. 4 The related parameters of dimples under three thicknesses (0.1, 0.2 and 0.3 mm) SIMP steel at enlargement factor 80000 times by SEM

Dimple	Mean size, μm	Mean depth, μm	Big dimples density, 1/μm^2	Evenness index
0.1 mm	0.264	0.226	7	Uneven
0.2 mm	0.453	0.792	15	General
0.3 mm	0.642	1.057	35	Uniform

Experimental results show that σ_y and σ_{UTS} can be well characterized by R_{mc}, R_{eHc} and $R_{tc0.5}$, and these may be linearized as follows (Ref 14, 21, 42, 43):

$$\sigma_{\mathrm{UTS}} = 0.0901\frac{F_m}{h_o^2} + 336.88 = -15.5345R_{mc} + 1899.028 = -15.5345R_{eHc} + 1899.028 \quad \text{(Eq 11)}$$

$$\sigma_y = 0.56\frac{F_e}{h_o^2} - 222.98 = 17.1254R_{tc0.5} + 108.824 \quad \text{(Eq 12)}$$

In addition, the elastic modulus ($E = 220.609$ GPa) of SIMP steel is obtained from SPT experiments by using Chica's method (Ref 21), it is very accurate compared to the theoretical values ($E = 211$ GPa). Most importantly, the values of σ_y, σ_{UTS} and E obtained with SPT experiments after the above handle are consistent with the results from the standard tensile tests, which

means that if the data of these parameters are substituted into Eq 1-5, the tensile test results can be easily reconstructed.

The shear stress analysis shows that the crack paths of SIMP steel specimens will form along the circumference and radial direction at RT, and the results are shown in Fig. 10(a), 13 and 14 and Table 3. Moreover, it is found by SEM micrographs that the specimen thickness does affect the cracking position of SPT experiments, and the results are shown in Fig. 10(b) and 15. Through the combination of the FEM calculation and SEM observation, it is obvious that the calculated results of the shear stress analysis are in good agreement with the SPT experimental results, and the errors are less than 3.2%. These indicate that FEM calculations can accurately obtain or simulate the parameters of SPT experiments. By comparing the FEM simulation results with the SPT experiment results, a large number of numerical tests are carried out on the FEM model for SIMP steel, the verification, validation and modification of this model are completed, and it fully ensures the validity and high credibility of the FEM model. Besides, it is also proved that the FEM model can be reasonably used to establish the data processing and analysis program for the SPT experiments.

The fracture energy calculated by FEM is compared with that of SPT experiments for the first time, and the errors between them are less than 9% are shown in Fig. 12. This further verifies the rationality of FEM simulations to establish the accepted program of SPT experimental data. Based on the long-term data accumulation of metallic materials, it is generally believed that the relationships between the fracture toughness (J_{IC}) of metals and the equivalent fracture strain and the maximum fracture energy density (W_{sp}^{m}) of metals are approximately linear (Ref 11, 13, 31, 48, 49). At present, this method is applicable to metallic materials and further verification is required as to whether it is applicable to other materials. Here, considering that the fracture toughness value of bulk materials measured by three-point bending tests is about 390 kJ/mm^2, the following empirical formula based on Shindo's methods (Ref 31) for J_{IC} versus W_{sp}^{m} can be obtained for SIMP steel:

$$J_{IC} = 440.4 W_{sp}^{m} - 120.86$$

W_{sp}^{m} is the maximum fracture energy density and taken by FEM calculation. Based on these, the FEM method is used to simulate SPT, which can easily and directly obtain the relatively accurate fracture toughness (J_{IC}) of SIMP steel through the maximum fracture energy density (W_{sp}^{m}). And, it is an engineering relationship between fracture toughness and the maximum fracture energy density. In addition, the following empirical formula based on Misawa's theories (Ref 48, 49) from the experimental point also can be presented for SIMP steel:

$$J_{IC} = 845\varepsilon_{qf} - 32.31$$

$$\varepsilon_{qf} = \ln\left(\frac{h_o}{h}\right)$$

where ε_{qf} is the equivalent fracture strain and taken by SPT experiments, h_o is the initial thickness, and h is the thinnest (the fracture) thickness of the specimen.

Shear stress is the main factor affecting the fracture properties of SPT experimental samples, and the shear stress distributions on the upper and lower surfaces of SIMP steel with three thicknesses are presented in Fig. 13, and the shear stress contour lines are also obtained as illustrated in Fig. 14. It is found that the shear stress on the upper and lower surfaces is greatly affected by the thickness, which is more intuitively proved by the shear stress isoline diagram. This explains that the size effect of miniature specimens should be considered when conducting SPT experiments. In fact, the grain size of SIMP steel is about 110 microns. The size effect will significantly increase the results when the thickness of the micro-tensile samples is reduced to a few grains. The above phenomenon can be perfectly fitted and explained by the strain gradient plasticity theory based on the dislocation mechanism developed by Nix and Gao (Ref 46, 47). Therefore, the theory of strain gradient plasticity based on dislocation mechanism should be introduced into FEM simulations to eliminate the influence of the size effect. SEM is used to observe the fracture morphology and structure of the SPT experimental samples for different thicknesses SIMP steel is depicted as in Fig. 15 and Table 4, and the results show that the dimple size, depth and density of SIMP steel become larger and more uniform with the increase in sample thickness. This indicates that the fracture resistance of SIMP steel has improved with the increase in sample thickness, and it reflects that the toughness of SIMP steel has improved. At the same time, this also indicates the size effect in miniature samples, and the thickness of the samples needs to be controlled accurately in SPT experiments. In addition, it is found that the shear stress isoline maps obtained by FEM and the dimple conditions of SIMP steel obtained by SEM can be used to characterize the same physical quantities, such as the elongation, hardness and stress state. Therefore, it is speculated that there has a certain relationship between the FEM shear stress contour maps and the SEM observed dimple situations.

The results calculated by the FEM of load–displacement curves do not completely fit with the SPT experimental results in the plastic instability stage are shown in Fig. 6, which is the same as the results (not completely fit in the plastic instability stage) obtained by Yang et al. (Ref 8). However, the errors between the SPT experiment results and the FEM simulation results without a damage model are very small. For example, all errors of the radial distance from the fracture to the center of the specimen between the FEM calculation results and the SEM observation results are less than 3.2%, and the errors of SP energy by FEM calculations and SPT experiments are inferior to 9% in SIMP steel samples of three thicknesses. So, the accuracy and reliability of the FEM simulation results are very high (at least greater than 95%) when the FEM simulations do not contain a damage model (Ref 34). Moreover, the focus of the current work is to establish the relationship of mechanical properties of standard tensile test samples derived from the data of SPT experiments and provide the method of establishing this relationship. So, there do not include a damage model in this research work. But if the appropriate parameters are selected and the Gurson–Tvergaard–Needleman (GTN) damage model of Martínez-Pañeda et al. is used for FEM simulations (Ref 50), and the results obtained are exactly the same as the experimental results. In other words, the problem of plastic instability stage can be modified by using a damage model (Ref 32-34, 50-53). Therefore, a damage model will be considered in future work. This will make the accuracy of the calculation results higher and the existing error (9%) even smaller. In addition, in order to study the irradiation damage effect, and the irradiation damage will be added to a damage model to analyze the constitutive relation of irradiation damaged materials.

The above results indicated that based on the shear stress analysis of FEM calculations, most mechanical properties of the materials, such as the elastic modulus (E), yield strength (σ_y), ultimate strength (σ_{UTS}), fracture energy (SP energy) and fracture toughness (J_{IC}), can be obtained accurately and directly through SPT experiments. On the other hands, these above findings also may improve the possibility of establishing a widely accepted program for obtaining basic materials properties from SPT experimental data by using FEM simulations and provide a new comparison scheme (or norm) for obtaining accurate data from miniature specimens. In addition, for the small size specimens which are difficult to carry out the traditional mechanical tests, SPT experiment combined with FEM analysis is an effective method to characterize the mechanical properties of materials and has great advantages and broad application prospects for material research in space, nuclear plant and other extreme environments.

5. Conclusions

The mechanical properties of φ3-mm disks miniature specimens of SIMP steel with different thicknesses (0.1, 0.2 and 0.3 mm) are investigated using the SPT experiments, FEM simulations and SEM observations. The following conclusions are drawn:

1. There is no difference in the load–displacement curves, SP energy, the distances between the maximum shear stress and the center of the specimens from SPT experiments and FEM calculations. Moreover, the FEM simulative results obtained by analyzing the shear stress distributions and the isoline maps agree well with the SEM observational results. The verification, validation and modification of the FEM model for SIMP steel are completed, and it fully ensures the validity and high credibility of this FEM model. Besides, it is also proved that the FEM model can be used precisely to establish the widely accepted analysis program of SPT experimental. The relationship of mechanical properties of standard tensile test samples derived from the data of small punch test is established, and the method of establishing this mechanical relationship is provided. Therefore, based on the shear stress analysis of FEM calculations, most mechanical properties of steels can be obtained directly through SPT experimental data.
2. On the basis of previous empirical formulas, the modified relationships among yield strength (σ_y), ultimate strength (σ_{UTS}), fracture toughness (J_{IC}) and compression strength (R_{mc}), upper compression yield strength (R_{eHc}), proof strength-total compression ($R_{tc0.5}$), maximum fracture energy density (W_{sp}^{m}) are built for SIMP steel, from which the tensile yield strength (σ_y), ultimate strength (σ_{UTS}) and fracture toughness (J_{IC}) of materials can be predicted directly by SPT experiments.
3. Considering that shear stress is the main factor affecting the fracture of SPT experimental samples, when the sample thickness is reduced to a certain degree, the size effect should be paid attention to in the miniature sample experiments. The theory of strain gradient plasticity based on dislocation mechanism should be introduced into FEM simulations to eliminate the influence of the size effect. In addition, the inconsistency problems at the plastic instability stage can be modified by using a damage model.

Acknowledgment

This research project was supported by the National Natural Science Foundation of China (NSFC) (Grant Nos. 12075293 and 91426304), the Instrument Developing Project of the Chinese Academy of Sciences (Grant No. E028341Y) and the Youth Innovation Promotion Association of the Chinese Academy of Sciences (Grant No. 2016365).

References

1. T.Y. Deng, J.R. Sun, P.T. Tai, Y.Y. Wang, L.Q. Zhang, H.L. Chang, Z.G. Wang, L.J. Niu, Y.B. Sheng, D.S. Xue, Q. Huang, Y.F. Zhou, P. Song and J.Y. Li, Ti_3AlC_2, a Candidate Structural Material for Innovative Nuclear Energy System: the Microstructure Phase Transformation and Defect Evolution Induced by Energetic Heavy-Ion Irradiation, *Acta Mater.*, 2020, **189**, p 188–203.
2. K.L. Murty and I. Charit, Structural Materials for Gen-IV Nuclear Reactors: Challenges and Opportunities, *J. Nucl. Mater.*, 2008, **383**, p 189–195.
3. D.E.J. Armstrong, C.D. Hardie, J.S.K.L. Gibson, A.J. Bushby, P.D. Edmondson and S.G. Roberts, Small-Scale Characterisation of Irradiated Nuclear Materials: Part II Nanoindentation and Micro-Cantilever Testing of Ion Irradiated Nuclear Materials, *J. Nucl. Mater.*, 2015, **462**, p 374–381.
4. T. Gozani, Active Nondestructive Assay of Nuclear Materials: Principles and Applications, *Nuclear Disarmament Safeguards & Physical Protection*, CR-0602, Vol 1, 1981, p 389–403 (in English)
5. K. Kumar, A. Pooleery, K. Madhusoodanan, R.N. Singh, J.K. Chakravartty, R.S. Shriwastaw, B.K. Dutta and R.K. Sinha, Evaluation of Ultimate Tensile Strength Using Miniature Disk Bend Test, *J. Nucl. Mater.*, 2015, **461**, p 100–111.
6. R.J. Lancaster, S.P. Jeffs, H.W. Illsley, C. Argyrakis, R.C. Hurst and G.J. Baxter, Development of a Novel Methodology to Study Fatigue Properties Using the Small Punch Test, *Mater. Sci. Eng., A*, 2019, **748**, p 21–29.
7. I.I. Cuesta, C. Rodriquez, F.J. Belzunce and J.M. Alegre, Analysis of Different Techniques for Obtaining Pre-Cracked/notched Small Punch Test Specimens, *Eng. Fail. Anal.*, 2011, **18**, p 2282–2287.
8. S. Yang, J. Zhou, X. Ling and Z. Yang, Effect of Geometric Factors and Processing Parameters on Plastic Damage of SUS304 Stainless Steel by Small Punch Test, *Mater. Des.*, 2012, **41**, p 447–452.
9. P. Dymáček, Recent Developments in Small Punch Testing: Applications at Elevated Temperatures, *Theor. Appl. Fract. Mech.*, 2016, **86**, p 25–33.
10. G.E. Lucas, The Development of Small Specimen Mechanical Test Techniques, *J. Nucl. Mater.*, 1983, **117**, p 327–339.
11. X. Mao and H. Takahashi, Development of a Further-Miniaturized Specimen of 3 Mm Diameter for Tem Disk (ø 3 Mm) Small Punch Tests, *J. Nucl. Mater.*, 1987, **150**, p 42–52.
12. G.E. Lucas, Review of Small Specimen Test Techniques for Irradiation Testing, *Metall. Trans. A*, 1990, **21**, p 1105–1119.
13. X. Mao, H. Takahashi and T. Kodaira, Supersmall Punch Test to Estimate Fracture Toughness JIc and Its Application to Radiation Embrittlement of 2.25Cr-1Mo Steel, *Mater. Sci. Eng., A*, 1992, **150**, p 231–236.
14. M. Bruchhausen, S. Holmström, I. Simonovski, T. Austin, J.-M. Lapetite, S. Ripplinger and F. de Haan, Recent Developments in Small Punch Testing: Tensile Properties and DBTT, *Theor. Appl. Fract. Mech.*, 2016, **86**, p 2–10.
15. G.E. Lucas, G.R. Odette, M. Sokolov, P. Spätig, T. Yamamoto and P. Jung, Recent Progress in Small Specimen Test Technology, *J. Nucl. Mater.*, 2002, **307**, p 1600–1608.

16. J.S. Lee, I.S. Kim and A.K. Kimura, Application of Small Punch Test to Evaluate Sigma-Phase Embrittlement of Pressure Vessel Cladding Material, *J. Nucl. Sci. Technol.*, 2003, **40**, p 664–671.
17. M. Abendroth and S. Soltysiak, Assessment of Material Properties by Means of the Small Punch Test, *Recent Trends Fract. Damage Mech.*, 2015, **1**, p 127–157.
18. E.N. Campitelli, P. Spätig, J. Bertsch and C. Hellwig, Assessment of Irradiation-Hardening on Eurofer97' and Zircaloy 2 with Punch Tests and Finite-Element Modeling, *Mater. Sci. Eng., A*, 2005, **400**, p 386–392.
19. P. Kumar, J. Chattopadhyay and B.K. Dutta, On the Correlation between Minimum Thickness and Central Deflection during Small Punch Test, *J. Nucl. Mater.*, 2016, **475**, p 37–45.
20. J. Zhong, Xu. Tong, K. Guan and J. Szpunar, A Procedure for Predicting Strength Properties Using Small Punch Test and Finite Element Simulation, *Int. J. Mech. Sci.*, 2019, **152**, p 228–235.
21. J.C. Chica, P.M. Díez and M.P. Calzada, Improved Correlation for Elastic Modulus Prediction of Metallic Materials in the Small Punch Test, *Int. J. Mech. Sci.*, 2017, **134**, p 112–122.
22. X. Jia and Y. Dai, Small Punch Tests on Martensitic/ferritic Steels F82H, T91 and Optimax-A Irradiated in SINQ Target-3, *J. Nucl. Mater.*, 2003, **323**, p 360–367.
23. Y. Dai, X.J. Jia and K. Farrell, Mechanical Properties of Modified 9Cr–1Mo (T91) Irradiated at $\leqslant$ 300 °C in SINQ Target-3, *J. Nucl. Mater.*, 2003, **318**, p 192–199.
24. C. Yang, T. Wei, O. Muránsky, D. Carr, H. Huang and X. Zhou, The Effect of Ball-Milling Time and Annealing Temperature on Fracture Toughness of Ni-3 wt.% SiC Using Small Punch Testing, *Mater. Charact.*, 2018, **138**, p 289–295.
25. Z.-X. Wang, H.-J. Shi, Lu. Jian, P. Shi and X.-F. Ma, Small Punch Testing for Assessing the Fracture Properties of the Reactor Vessel Steel with Different Thicknesses, *Nucl. Eng. Des.*, 2008, **238**, p 3186–3193.
26. P. Kubík, F. Šebek, J. Petruška, J. Hůlka, N. Park and H. Huh, Comparative Investigation of Ductile Fracture with 316L Austenitic Stainless Steel in Small Punch Tests: Experiments and Simulations, *Theor. Appl. Fract. Mech.*, 2018, **98**, p 186–198.
27. K. Song, L. Zhao, Xu. Lianyong, Y. Han and H. Jing, Experimental and Numerical Analysis of Creep and Damage Behavior of P92 Steel by Small Punch Tests, *Theor. Appl. Fract. Mech.*, 2019, **100**, p 181–190.
28. L. Zhao, K. Song, L. Xu, Y. Han, H. Jing, Y. Zhang and H. Li, Determination of Creep Properties of an Advanced Fe-Cr-Ni Alloy Using Small Punch Creep Test with a Modified Creep Strain Model, *Theor. Appl. Fract. Mech.*, 2019, **104**, p 102324.
29. L. Zhao, K. Song, L. Xu, Y. Han, H. Jing, H. Li and Y. Zhang, Investigating Creep Rupture and Damage Behavior of 41Fe-25.5Cr-23.5Ni Alloy Small Punch Creep Specimens Using a Novel Microstructure Meshing Approach, *Mater. Sci. Eng., A*, 2019, **766**, p 138370.
30. I. Simonovski, S. Holmström and M. Bruchhausen, Small Punch Tensile Testing of Curved Specimens: Finite Element Analysis and Experiment, *Int. J. Mech. Sci.*, 2017, **120**, p 204–213.
31. Y. Shindo, K. Horiguchi, T. Sugo and Y. Mano, Finite Element Analysis and Small Punch Testing for Determining the Cryogenic Fracture Toughness of Austenitic Stainless Steel Welds, *J. Test. Eval.*, 2000, **28**, p 431–437.
32. I. Simonovski, S. Holmström, D. Baraldi and R. Delville, Investigation of Cracking in Small Punch Test for Semi-Brittle Materials, *Theor. Appl. Fract. Mech.*, 2020, **108**, p 1–12.
33. T. Gao, L. Ying, Hu. Ping, X. Han, H. Rong, Wu. Yi and J. Sun, Investigation on Mechanical Behavior and Plastic Damage of AA7075 Aluminum Alloy by Thermal Small Punch Test: Experimental Trials, Numerical Analysis, *J. Manuf. Process.*, 2020, **50**, p 1–16.
34. L. Xue, X. Ling and S. Yang, Mechanical Behaviour and Strain Rate Sensitivity Analysis of TA2 by the Small Punch Test, *Theor. Appl. Fract. Mech.*, 2019, **99**, p 9–17.
35. K. Liu and S.N. Melkote, Material Strengthening Mechanisms and Their Contribution to Size Effect in Micro-Cutting, *J. Manuf. Sci. Eng.*, 2006, **128**, p 730.
36. G. Simons, C. Weippert, J. Dual and J. Villain, Size Effects in Tensile Testing of Thin Cold Rolled and Annealed Cu Foils, *Mater. Sci. Eng., A*, 2006, **416**, p 290–299.
37. M. Rund, R. Procházka, P. Konopík, J. Džugan and H. Folgar, Investigation of Sample-Size Influence on Tensile Test Results at Different Strain Rates, *Proc. Eng.*, 2015, **114**, p 410–415.
38. J. Henry, S.A. Maloy, Irradiation-resistant ferritic and martensitic steels as core materials for Generation IV nuclear reactors, *Structural Materials for Generation IV Nuclear Reactors*, Vol 1, 2017, p 329–355 (in English)
39. J. Liu, Q. Shi, H. Luan, W. Yan, W. Sha, W. Wang, Y. Shan and K. Yang, Oxidation and Tensile Behavior of Ferritic/martensitic Steels after Exposure to Lead-Bismuth Eutectic, *Mater. Sci. Eng., A*, 2016, **670**, p 97–105.
40. C. Liu, M.-C. Zhao, T. Unenbayar, Y.-C. Zhao, B. Xie, Y. Tian, Y.-Y. Shan and K. Yang, Hot Deformation Behavior of a New Nuclear Use Reduced Activation Ferritic/martensitic Steel, *Acta Metall. Sin. (english Letters)*, 2018, **32**, p 825.
41. P. Jin, T. Shen, M. Cui, Y. Zhu, B. Li, T. Zhang, J. Li, S. Jin, Lu. Eryang, X. Cao and Z. Wang, Study on Vacancy-Type Defects in SIMP Steel Induced by Separate and Sequential H and He Ion Implantation, *J. Nucl. Mater.*, 2019, **520**, p 131–139.
42. M. Bruchhausen, E. Altstadt, T. Austin, P. Dymacek, S. Holmström, S. Jeffs, R. Lacalle, R. Lancaster, K. Matocha and J. Petzova, European Standard on Small Punch Testing of Metallic Materials, *Ubiq. Proc.*, 2018, **1**, p 11.
43. K. Matocha and R. Hurst, Small Punch Testing—The Transition from a Code of Practice to a European Testing Standard, *Key Eng. Mater.*, 2017, **734**, p 3–22.
44. B. Yang, F.-Z. Xuan and J.-K. Chen, Evaluation of the Microstructure Related Strength of CrMoV Weldment by Using the in-Situ Tensile Test of Miniature Specimen, *Mater. Sci. Eng., A*, 2018, **736**, p 193–201.
45. H. Ge, L. Peng, Y. Dai, Q. Huang and M. Ye, Tensile Properties of CLAM Steel Irradiated up to 20.1 Dpa in STIP-V, *J. Nucl. Mater.*, 2016, **468**, p 240–245.
46. W.D. Nix and H. Gao, Indentation Size Effects in Crystalline Materials: A Law for Strain Gradient Plasticity, *J. Mech. Phys. Solids.*, 1998, **46**, p 411–425.
47. H. Gao, Y. Huang, W.D. Nix and J.W. Hutchinson, Mechanism-Based Strain Gradient Plasticity—I. Theory, *J. Mech. Phys. Solids.*, 1999, **47**, p 1239–1263.
48. T. Misawa, S. Nagata, S. Aoki, J. Ishizaka and Y. Hamaguchi, Fracture Toughness Evaluation of Fusion Reactor Structural Steels at Low Temperatures by Small Punch Tests, *J. Nucl. Mater.*, 1989, **169**, p 225–232.
49. P. Kumar, B.K. Dutta and J. Chattopadhyay, Numerical Development of a New Correlation between Biaxial Fracture Strain and Material Fracture Toughness for Small Punch Test, *J. Nucl. Mater.*, 2017, **486**, p 332–338.
50. E. Martínez-Pañeda, I.I. Cuesta, I. Peñuelas, A. Díaz and J.M. Alegre, Damage Modeling in Small Punch Test Specimens, *Theor. Appl. Fract. Mech.*, 2016, **86**, p 51–60.
51. I.I. Cuesta, J.M. Alegre and R. Lacalle, Determination of the Gurson–tvergaard Damage Model Parameters for Simulating Small Punch Tests, *Fatigue. Fract. Eng. m.*, 2010, **33**, p 703–713.
52. H.T. Pham and T. Iwamoto, An Evaluation of Fracture Properties of Type-304 Austenitic Stainless Steel at High Deformation Rate Using the Small Punch Test, *Int. J. Mech. Sci.*, 2018, **144**, p 249–261.
53. W. Wen, G.A. Jackson, H. Li and W. Sun, An Experimental and Numerical Study of a CoNiCrAlY Coating Using Miniature Specimen Testing Techniques, *Int. J. Mech. Sci.*, 2019, **157**, p 348–356.

Publisher's Note Springer Nature remains neutral with regard to jurisdictional claims in published maps and institutional affiliations.